PERIODICUM BIOLOGORUM
VOL. 125, No 1–2, 101–113, 2023
DOI: 10.18054/pb.v125i1-2.24080

UDC 57:61
CODEN PDBIAD
ISSN 0031-5362

Review

Use of atomic force microscopy for characterization of model membranes and cells

ANJA SADŽAK
LUCIJA MANDIĆ
VIDA STRASSER
SUZANA ŠEGOTA*

Laboratory for Biocolloids and Surface Chemistry, Division of Physical Chemistry, Ruđer Bošković Institute, Zagreb, Croatia

***Correspondence:**
Suzana Šegota
E-mail address: Suzana.Segota@irb.hr

Keywords: atomic force microscopy; AFM; SPM; imaging; force spectroscopy; nanomechanics; roughness parameters

Abbreviations

AFM	– atomic force microscopy
SPM	– scanning probe microscopy
STM	– scanning tunnelling microscopy
DMPC	– 1,2-dimyristoyl-sn-glycero-3-phosphocholine
SLB	– supported lipid bilayer
PBS	– phosphate buffered saline buffer
SW	– seawater
/	– ionic strength
SH-SY5Y	– neuroblastoma cell line from a metastatic bone tumor cells
P19	– neurons from teratocarcinoma cell lines
ROS	– reactive oxygen species

Received November 20, 2022
Revised January 31, 2023
Accepted May 5, 2023

Abstract

Background: *To provide a fundamental understanding of the potential and use of atomic force microscopy (AFM) in medicine and the life sciences, this work presents a thorough description of imaging and non-imaging atomic force microscopy modes for characterizing model membranes and cells at the nanoscale.*

Methods: *The imaging and non-imaging AFM modes are described with examples in terms of the characterization of topographic, morphological, and nanomechanical sample properties.*

Results: *AFM imaging of supported lipid bilayers (SLBs) revealed the effects of temperature and medium composition on SLB topography in the gel and fluid phases, and on the bilayer thickness. Non-imaging AFM showed the strengthening of the SLB in both phases by the ion binding process.*

Imaging of neuronal and neuroblastoma cells with and without treatment revealed morphological changes in shape, volume, roughness, and Feret dimension. Non-imaging AFM showed the change in cell elasticity induced by the treatment with H_2O_2 with and without quercetin and by the treatment with copper and myricetin. The measurements of cells elasticity revealed a reorganization of the cytoskeleton and filament structures.

Conclusions: *Diverse applications of imaging and non-imaging AFM can provide important information about the underlying processes in biologically relevant systems. AFM, as a complementary technique to other biomedical methods, allows screening and monitoring of physiological changes at the nanoscale.*

INTRODUCTION

Atomic force microscopy (AFM) is a lens-free technique that can achieve sub-nanometer resolution on biospecimens under physiological conditions. AFM measures the atomic forces that occur between the sample and the probe. AFM is capable of simultaneously obtaining a set of height data, which is converted into an image, and a set of nanomechanical data characterizing the investigated sample. The main advantage of this technique is the ability to image both solid and liquid samples in native form at ambient conditions without the required vacuum *(1,2)*. Gerd Binnig and Heinrich Rohrer received the Nobel Prize in physics for the development of the scanning tunneling microscope (STM), a technique that is related to AFM and belongs to the group of scanning probe microscopies (SPM), which highlights the innovation and importance of such methods. Today, AFM is a widely used

technique for imaging, measuring nanomechanical properties and manipulation at the nanoscale which enables tackling problems in many scientific fields, from nanotechnology, chemistry, and physics of materials to colloid and surface chemistry, pharmacy, molecular and cell biology, and medicine *(3-5)*.

Using selected examples from our research, here we provide an introduction to readers with a background in biology and medicine into the potential of the AFM technique and its ability to provide more information than a simple representation of the sample topography. We begin with a description of the basic concepts and operation of the AFM instrument. We then explain the parameters that can be obtained from the measurements, which are relevant to the research presented further in this review. In the third section, a brief overview of the imaging of the model lipid 1,2-dimyristoyl-sn-glycero-3-phosphocholine (DMPC) membrane-supported lipid bilayer (SLB) in liquid cells will be presented. In addition, the application of force spectroscopy in the study of SLB is shown to illustrate how physicochemical properties and processes at the nanoscale can be resolved using results from AFM measurements, e.g., the bilayer thickness, coverage of the support surface, and the yield threshold force. The fourth section describes the studies of neuroblastoma cell lines derived from metastatic bone tumor (SH -SY5Y) and teratocarcinoma cell lines (P19 neurons), where the imaging mode was used to gain insight into the state of the cells based on cell morphology, membrane roughness, and dimensional parameters (Feret dimension). The non-imaging mode was used to determine cell elasticity as one of the biophysical markers for assessing the condition of the studied cells.

FUNCTIONAL PRINCIPLE OF THE AFM

Basic configuration of the AFM device

The AFM consists of a cantilever with a sharp tip attached to the end, which is used to scan the sample surface. As the tip approaches the sample surface, forces occur between the probe tip and the sample, causing deflection of the cantilever according to Hooke's law *(6)*. Depending on the distance between the probe and the sample, AFM measures Van der Waals forces (at distances of 1-10 nm above the surface), electrostatic forces, or other long-range forces that extend across the surface. An example of forces that can be measured with AFM are Van der Waals forces between lipid molecules in lipid bilayers and electrostatic forces between ions present in the medium and the polar heads of the lipid molecules in the lipid bilayer, which occur in media with high ionic strength such as seawater (SW) *(7)*.

Figure 1 shows the basic parts of the AFM instrument: a small spring-shaped cantilever (1) supports a sharp tip attached to its free end (2). The tip is used to probe the

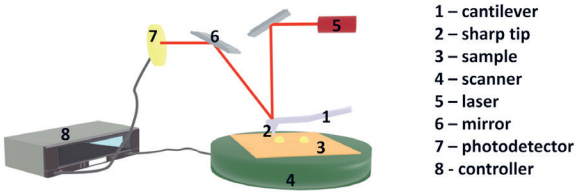

Figure 1. *Schematic representation of a typical AFM configuration.*

sample at the nanometer scale (3). The sample is placed on the scanner head (4) which moves the sample in x, y and z directions. The laser beam (5) is reflected from the surface of the cantilever and reaches the photodetector (7) via a mirror system (6), which detects the deflection of the cantilever. The electrical signal at the photodetector is regulated by the controller (8). In this way, the interaction between the tip and the sample is translated into changes in the movement of the cantilever in the form of the deflection value, the amplitude of the cantilever oscillation, or the shift in the resonant phase of the cantilever oscillation. AFM scanners consist of a piezoelectric material that expands and contracts in response to an applied voltage. The tip or sample is placed on the piezoelectric scanner, which moves in the x, y, and z directions *(8)*. The scanners are characterized by their sensitivity, i.e., the ratio of expansion or contraction of the piezoelectric material per applied voltage. Sensitivity varies from scanner to scanner, but piezo scanners show higher sensitivity at the end of the scan than at the beginning of the scan. The hysteresis between the two scan directions *(9)* should be corrected using established scanner calibration procedures *(10,11)*.

Types of probes

The AFM probe consists of a micrometer-long spring cantilever made of Si, SiO_2, or Si_3N_4 with a sharp tip (radius of curvature in the order of nanometers) attached to the lower part of the cantilever. The surface of the cantilever can be modified with various coatings to increase the reflection of the laser beam incident on the cantilever and improve the deflection signal *(12)*. The spring constants are in the range of 10^{-2} N/m ≤ k_s ≤ 100 N/m and oscillation

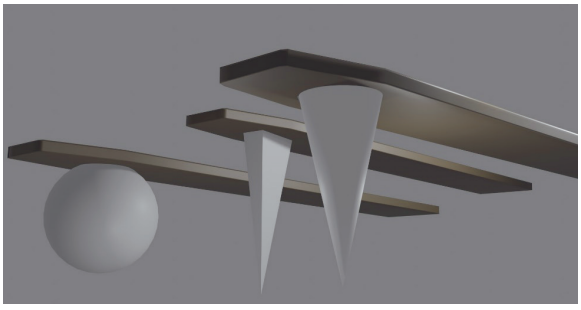

Figure 2. *Schematic representation of AFM cantilevers with spherical, pyramidal and conical tips (from left to right).*

frequencies of 1 kHz ≤ ω_0 ≤ 500 kHz, while the geometry can be triangular or rectangular. The tip radius of the probe is usually in the order of a few nanometers to a few tens of nanometers. There are special probes, such as colloidal probes with spherical tips, with much larger radii (Figure 2). By scanning a sample with an AFM probe, different types of interactions can be detected. Depending on the investigated interaction, the surface of the AFM cantilever tip can be modified by a coating.

AFM imaging modes

In general, the possible imaging modes are divided into contact and non-contact modes. A widely used non-contact imaging mode is known as the "tapping" mode (*13*). Depending on the distance between the tip and the sample surface, attractive or repulsive forces occur, and different imaging modes can be applied, as shown in Figure 3.

Contact mode

In a contact mode, the probe is in constant contact with the sample surface at a very close distance. Therefore, in contact mode, AFM is performed at a distance where the force is in the repulsive range (Figure 3). In this mode, it is possible to image either at constant force or at constant distance. The topography is thus measured by the deflection of the cantilever (*14*). Since the contact mode is usually used for measuring hard samples and materials, it will not be considered further in the discussion on imaging of biological samples.

Tapping mode

The tapping mode, as the most commonly used AFM mode in both ambient and liquid environments, was designed to avoid damage of soft samples, for example films, membranes, or cells *(12)*. The cantilever oscillates at its constant resonant frequency resulting in a constant oscillation amplitude as long as there is no interaction with the sample surface *(13)*. As the probe tip approaches the sample, the interaction forces induce a decrease of the cantilever amplitude (Figure 3). The feedback controller then returns the cantilever amplitude to the initial constant value, and the amount of this feedback is quantified. Imaging in the tapping mode is gentle enough to visualize even supported lipid bilayers in liquid media *(15-18)*. The interaction between the tip and the sample also causes a shift in the phase of the cantilever oscillation, allowing detection of sample regions with different chemical, stiffness, or adhesion properties *(19)*.

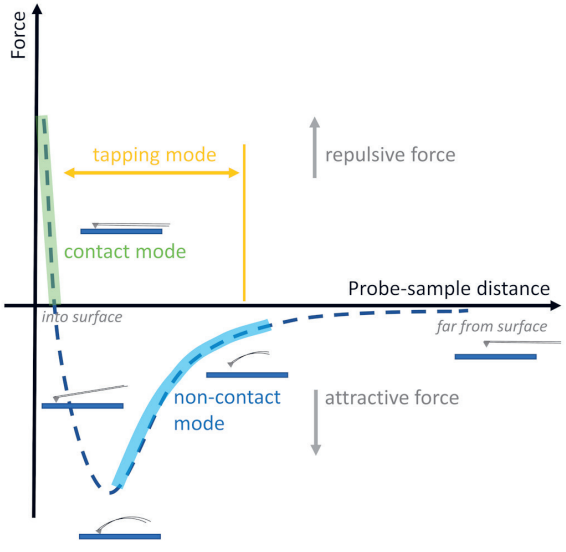

Figure 3. *Force-distance curve. Redrawn after (12).*

Non-contact mode

The main difference between non-contact and tapping modes is the frequency of the cantilever oscillation, which in the non-contact mode is slightly higher than its resonant frequency, while the amplitude of the oscillation is in the range of a few picometers to a few nanometers (*20*). At these distances, the reduction in the resonant frequency of the cantilever is determined by the Van der Waals force or other long-range forces that extend across the surface (*21*). In the non-contact AFM, neither the tip nor the sample is damaged (Figure 3). Therefore, non-contact AFM is used to image soft samples, such as membranes and cells, or thin, soft films. The so-called dynamic mode of AFM measurements includes frequency and amplitude modulation. While changes in the oscillation frequency provide information about probe-sample interactions (*22*), changes in the oscillation phase allow distinction between regions having different material composition on a sample surface (*23*).

Roughness parameters

AFM imaging mode allows the determination of several roughness parameters, used to evaluate the surface topography, especially in cell studies.

Roughness Average, R_a, is the arithmetic mean of the absolute values of the profile height over the evaluation length. It is defined as:

$$R_q = \sqrt{\frac{1}{n}\sum_{i=1}^{n} y_i^2}$$

where y_i represents the vertical deviations of the height profiles from the main plane, while R_q, is the root mean square average of the profile heights over the evaluation length, defined as:

$$R_q = \sqrt{\frac{1}{n}\sum_{i=1}^{n} y_i^2}$$

The Z range is the maximum distance between the highest and the lowest point on the scanned surface *(24)*. Examples of the application of roughness analysis in our previous cell studies can be found in chapters *SH-SY5Y cells* and *P19 neuronal cells*.

Cell morphology analysis

A method used to describe cell morphology involves determination of the maximum, F_{max}, and the minimum Feret dimension, F_{min}, as the maximum and minimum distance between two parallel lines tangential to the boundary line of the region of interest *(25)*. F_{max} and F_{min} are shown schematically in Figure 4.

Non-imaging mode – Force spectroscopy

The non-imaging mode, also known as force spectroscopy (FS), measures the forces between the sample and the probe as a function of their mutual distance. In FS, the AFM tip is extended to the surface and then retracted. The result of this measurement is called the force-displacement curve or the force-distance curve *(26-29)*. FS is generally used to measure the nanomechanical properties of samples, such as Young's modulus (E) and yield threshold force, which are related to material's stiffness *(30)*.

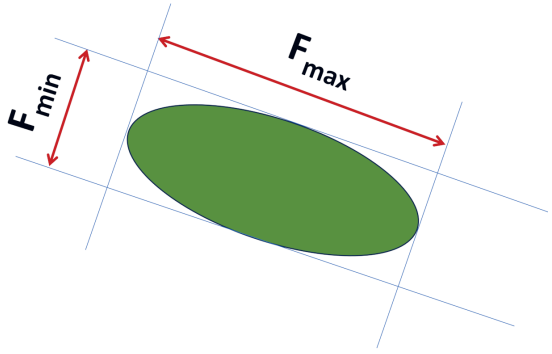

Figure 4. *Schematic illustration of F_{max} and F_{min}.*

MODEL MEMBRANES

In our previous work, we demonstrated mutual effects of monovalent (sodium) and divalent (calcium and magnesium) cations on the nanomechanics of 1,2-dimyristoyl-sn-glycero-3-phosphocholine (DMPC) bilayers in a buffer solution (PBS) and seawater (SW) *(7)*.

The binding effect of ions present in the medium is an important process leading to a change in the nanomechanical properties of the membrane. Supported lipid bilayer (SLB) was used as a model system because it behaves similarly to the cell membrane and has both fluid and gel phases. DMPC is the most abundant phospholipid in basolateral gill membranes and accounts for 61% of the total membrane phospholipid content in both freshwater and SW organisms. DMPC is also present in the yellow and brown leaves of the mangrove *Avicennia marina (31)*. It has a phase transition temperature from gel to fluid phase at 24.3 °C *(32)*. Due to ionic bonding, it has also been studied with AFM imaging and force spectroscopy. The SLB is formed by the process shown in Figure 5. The DMPC liposomes adhere to the mica surface, attach to it, spread, and adsorb to the mica surface, forming the SLB. SLBs consist of two main phases, the gel or solid phase and the liquid or fluid phase, which have different physical properties (thickness, fluidity, elasticity, stiffness, etc.), which determine their different behavior (Figure 6). The change in SLB nanomechanics, i.e., stiffness, is quantified in AFM by the yield threshold force defined as the vertical force required to penetrate DMPC SLB with the AFM probe.

The yield threshold force can be obtained from the force curve, which increases as the probe tip approaches the membrane surface. When the force is high enough, a jump appears in the force curve as shown in Figure 7. The breakthrough feature (known as a jump) corresponds to the penetration of the bilayer (yield threshold force), while the width of the jump corresponds to the thickness of the

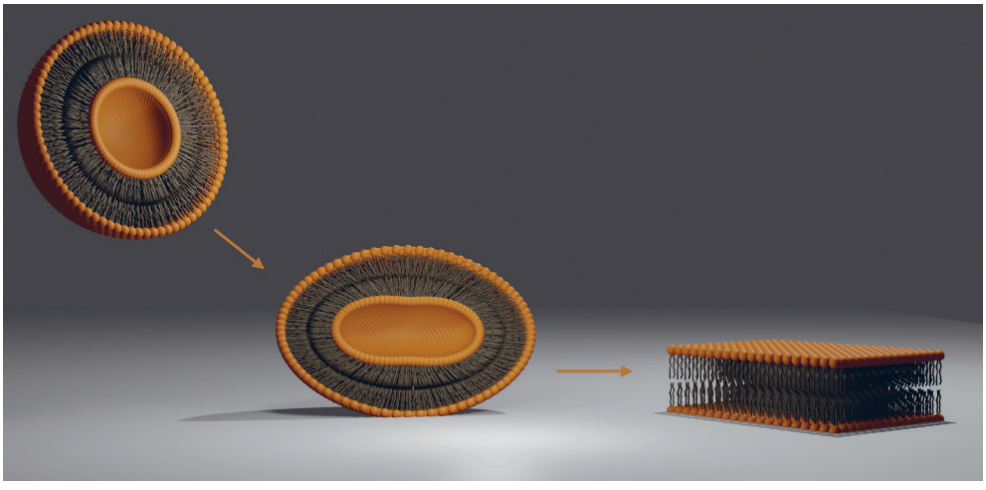

Figure 5. *Schematic representation of the formation of a SLB.*

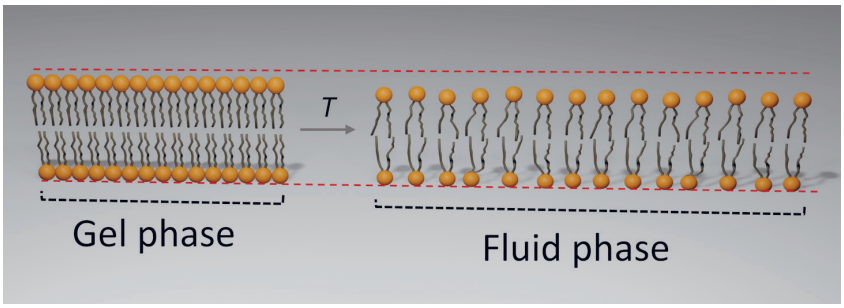

Figure 6. *Schematic representation of the temperature induced gel to fluid phase transition in the SLB.*

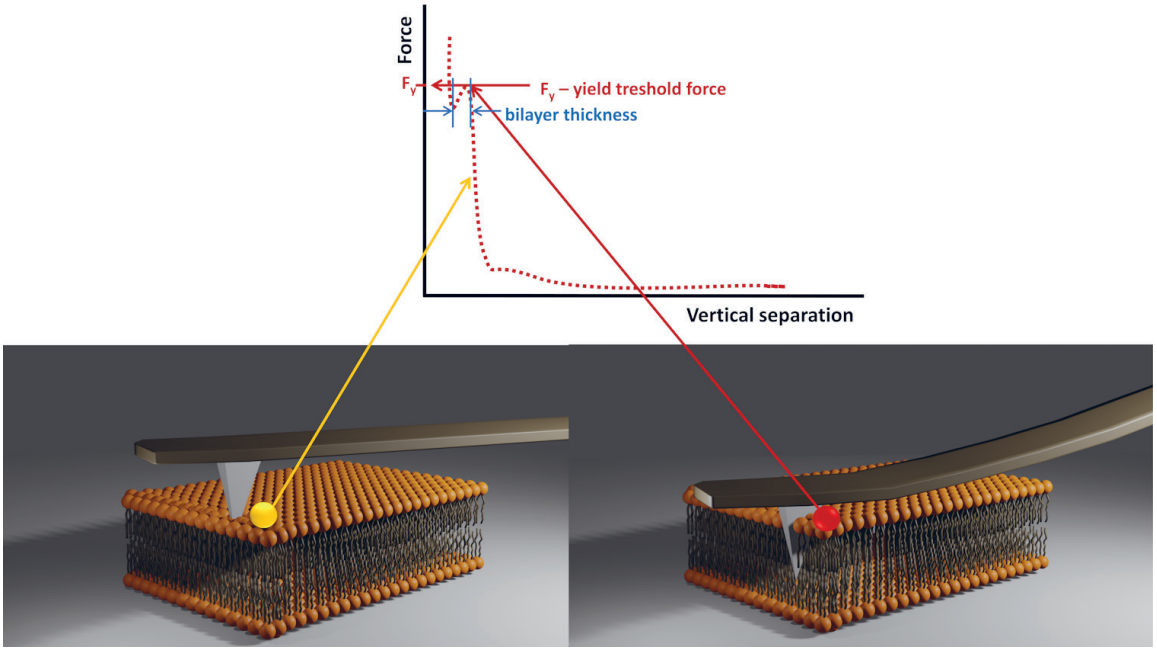

Figure 7. *Schematic representation of the "jump" in the force curve.*

charged membrane. Measuring these two features gives the local SLB property, which is measured at one point. For this reason, such measurements are made in different areas of the SLB to obtain information about the homogeneity of the specimen.

Collecting many yield threshold forces from different areas of the SLB patches (Figure 8A) resulted in the histogram of yield threshold forces shown schematically in Figure 8B. A unimodal distribution of the measured yield threshold force values and its small standard deviation

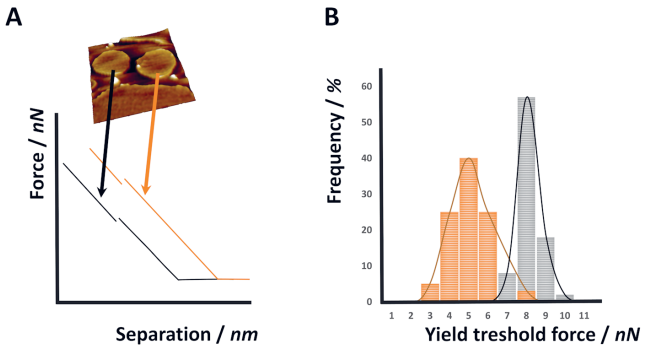

Figure 8. *Schematic representation of the collected force curves (A) and the histogram of yield threshold forces usually obtained from different regions on the patches (B).*

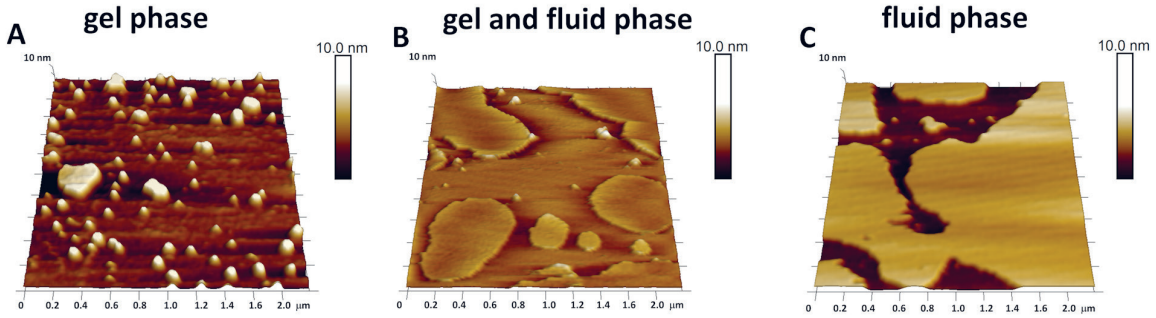

Figure 9. *3D-AFM images of DMPC SLB in PBS buffer (I = 150 mM) at temperatures of (A) 21.1 °C, (B) 24.3 °C and (C) 29.2 °C.*

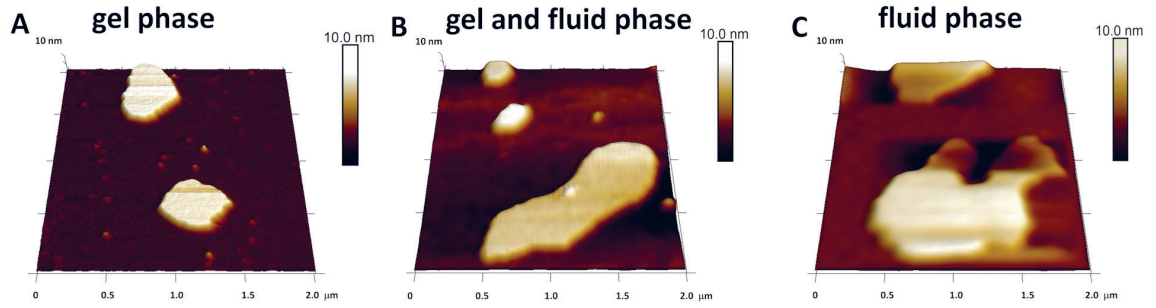

Figure. 10. *3D AFM images of supported DMPC bilayer in SW at temperatures of (A) 21.1 °C, (B) 24.3 °C and (C) 29.2 °C.*

indicates that the SLB is more or less homogeneous, i.e., only one phase is probably present, whereas a wide distribution of yield threshold forces or the occurrence of a bimodal distribution indicates the heterogeneity of the SLB and/or the presence of two phases.

AFM imaging – coverage of the supporting mica surface

Here we briefly show how AFM imaging of DMPC SLB in liquid cells can be used to study the physicochemical properties and processes on the nanoscale flat surface of mica. AFM imaging of SLB at different temperatures in two media, PBS buffer and SW, was performed to reveal the effects of ionic composition and temperature on DMPC SLB fusion and deposition in both gel and liquid phases, as described in our original study *(7)*. The liposome adsorption process resulted in the formation of SLB patches of different sizes and topographies at different temperatures in PBS and in SW (Figure 9 and Figure 10, respectively).

Sodium and potassium cations are present in the PBS buffer and bind to the DMPC head groups. At pH 7.4, the mica surface is negatively charged, and at the same pH, the DMPC liposomes are also slightly negatively charged. At 21.1 °C, the DMPC is in the gel phase, where ionic binding is lower. Therefore, the electrostatic interactions between the DMPC liposomes and the mica surface are weak, resulting in low surface coverage (Figure 9A). At higher temperatures, 24.3 °C and 29.2 °C, the DMPC is in fluid phase and ionic binding is enhanced, which is reflected in a lower negative DMPC surface charge and enhanced electrostatic interaction between DMPC and the mica support. As a result, a higher degree of mica coverage is observed, as shown in Figure 9B and Figure 9C. In SW, divalent cations such as calcium and magnesium are present in addition to sodium and potassium ions. Their binding to the surface of the bilayer enhances the interaction between DMPC and the mica support, resulting in increased coverage of the mica surface in the gel phase at 21.1 °C (Figure 10A), and in the fluid phase at 24.3 and 29.2 °C (Figure 10B, 10C).

Non-imaging AFM - determination of the bilayer thickness

The determination of the thickness of the lipid bilayer based on the width of the jump in the force – distance curve has already been described in section 3. By measuring many curves, the mean value of the thickness is ob-

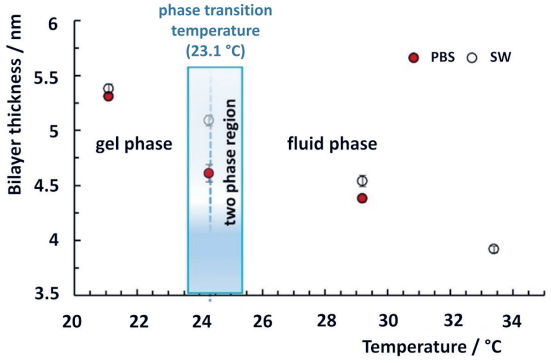

Figure 11. *Temperature dependence of the SLB thickness in PBS and SW media.*

tained, which depends on whether DMPC SLB is in the gel or the fluid phase. The measurement results are shown in Figure 11.

The change in the thickness of the bilayer is composed of two contributions, the phase transition itself and the binding of ions specific to PBS and SW. The thickness of the DMPC bilayer in the gel phase is practically the same as in PBS and SW, d = (5.31 ± 0.02) nm and d = (5.38 ± 0.04) nm, respectively. In the fluid phase, however, the thickness of the bilayer in PBS and SW is d = (4.38 ± 0.03) nm and d = (4.54 ± 0.05) nm, respectively. It can be seen that the difference in the thickness of the bilayer between PBS and SW is very small in the gel phase, while it is larger in the fluid phase due to the effect of enhanced binding of the ions present in the fluid phase. On the other hand, this difference is by far the largest in the phase transition region, as can be seen in Figure 11, which is due to the largest contribution of the phase transition itself, while the effect of ion binding in PBS and SW is much smaller in this temperature range. The results of the SLB thickness measurements are summarized in Figure 11. They suggest that the reduced thickness of the bilayer corresponds to the phase transition from gel to fluid and to the effects of binding of hydrated divalent cations (Ca^{2+} and Mg^{2+}) in SW to the lipid head groups. The observed difference in the thickness of the bilayer in two different media further confirms the effect of ionic binding.

Non-imaging AFM – determination of the yield threshold force

Changes in the SLB nanomechanical properties can be quantified by the yield threshold force, which is the vertical force required to penetrate DMPC SLB with an AFM probe. Due to the ionic binding, there is a strengthening of SLB, which should also be reflected in an increase in the yield threshold values. The divalent ions are present in SW at relatively low concentrations ($c(Ca^{2+})$ = 10.4 mM, $c(Mg^{2+})$ = 53.3 mM), whereas the monovalent ions are present at higher concentrations ($c(Na^{+})$ = 0.47 M, $c(Cl^{-})$ = 0.55 M) *(33)*. However, the effect of ion binding is much smaller in the fluid than in the gel phase and the decrease of the yield threshold force is linear with the temperature increment in both media, but a higher slope is observed in SW. The difference between the maximum yield threshold forces in the two media was larger in the gel phase than in the fluid phase, which can be attributed to the higher electrostatic interactions of the head groups in the gel phase of DMPC SLB (Figure 12). We have briefly shown how the FS measurement can be useful for the quantitative description of the process of membrane stiffening due to the binding of individual monovalent and divalent cations at the surface of the lipid bilayer. This finding could be applied not only to the DMPC bilayers in various media, but also to the analysis of the behavior of biological membranes in general.

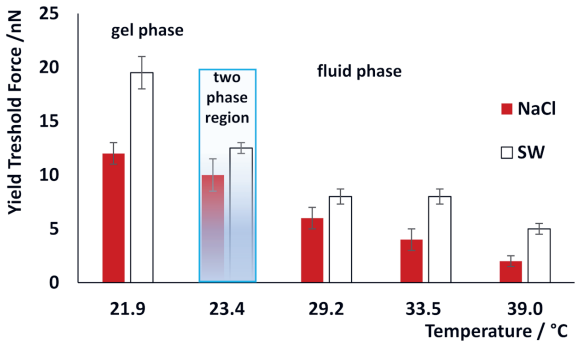

Figure 12. *Histogram of the yield threshold forces, F_y, as a function of temperature in NaCl and SW. Each value represents the central value of the Gaussian fit of the corresponding distribution while the error bars correspond to the standard deviations.*

CELLS

It is well known that the physiological functions of a cell are closely related to its morphology. When a toxin or drug is introduced, molecular changes occur inside the cell, in addition to changes in the cell morphology, especially of its nanomechanical properties. The SH-SY5Y neuroblastoma cell line and the P-19 neuronal cell line are routinely used to study various aspects of neuronal biology, including the cellular response to oxidative stress-induced injury.

SH-SY5Y cells

Oxidative stress (OS) causes neuronal damage and loss of function and has been linked to Alzheimer's and Parkinson's disease, mainly due to an imbalance of various transition metals (34). An increased concentration of free copper ions leads to induced oxidative stress and can cause direct and non-specific binding to various cellular proteins, resulting in protein folding (35). Although flavonoids are natural compounds that serve as therapeutic agents against oxidative damage, they may exhibit pro-oxidant activity, especially in the presence of metal ions (36). Myricetin is a flavonoid belonging to the flavonols group with antioxidant and anti-inflammatory activity (37), but in the presence of copper ions, myricetin can exhibit pro-oxidant behavior. In our recently published study (34), we investigated the protective role of the flavonoid myricetin in copper-induced toxicity in neuroblastoma cells SH-SY5Y. Here, we provide an overview of how both imaging and non-imaging AFM modes provide valuable information about the changes in cell membranes and cytoskeletal architecture that result from cell exposure to oxidative stress. The imaging AFM was used to visualize the cell morphology, while the non-imaging mode revealed the cell nanomechanics, i.e., the elasticity of cells.

Imaging AFM

In the original study *(38)*, we used AFM imaging to show detailed morphological changes in neuroblastoma cells SH -SY5Y after treatment with 10 μg/mL myricetin or 0.5 mM $CuSO_4$ and simultaneous administration of both agents. The 3D topography of control cells (Figure 13A), myricetin treated cells (Figure 13B), cells treated with copper (Figure 13C), and cells treated with copper and myricetin (Figure 13D) showed relatively clear and distinct details. The observed changes in morphology and surface roughness represent the reorganization of fine actin-filament structures leading to the formation of clusters of membrane protrusions. On control cells, the protrusions exhibited organized filaments up to 100 nm high, clearly separated from each other and homogeneously distributed over the entire scan area, forming cavities between them (Figure 13A). After treatment with myricetin, filaments with a smaller cavity between them were still observed. Although the treatment with myricetin did not significantly change the roughness parameters R_a and R_q, the Z area increased by 30%. After treatment with copper, the ordered filaments disappeared, but newly formed clusters of membrane protrusions, which were inhomogeneously distributed on the cell surface, could be a consequence of the signaling response of the ordered structure of the filaments to the external environment. These newly formed membrane protrusions cover about 45% of the cell surface. When treated simultaneously with myricetin and copper, the membrane protrusions covered approximately 85% of the cell surface (Figure 13D). The observed changes in surface morphology are reflected in the further increase in surface roughness parameters (Figure 14A), indicating that the fine filament structure is seriously damaged and that the process of reorganization of the fine filament structures of SH-SY5Y cells has progressed.

Surface roughness analysis was performed on the morphology of neuroblastoma SH-SY5Y control and treated cells in eight selected areas of 25 μm^2 (Figure 14A). The data showed the change in surface roughness due to different treatments. For example, the copper-treated cell surface was significantly rougher, indicating the formation of membrane protrusions on the cell surface, which increased the values of Z-range, R_q, and R_a by 46%, 40%, and 64%, respectively. The increase in all roughness parameters was observed in all treatments, with the change

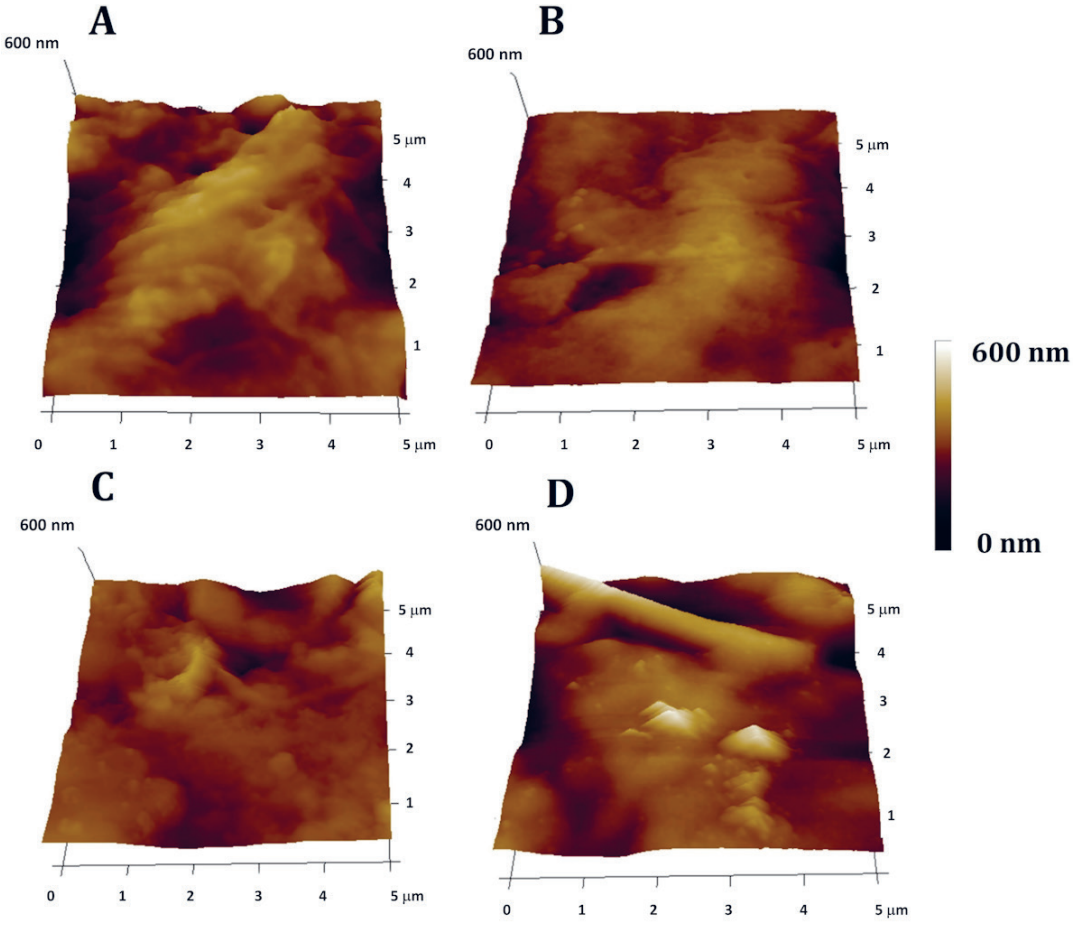

Figure 13. *3D topography images of parts of neuroblastoma SH-SY5Y cells: control cell (A), myricetin treated cell (B), copper treated cell (C), and myricetin and copper treated cell (D).*

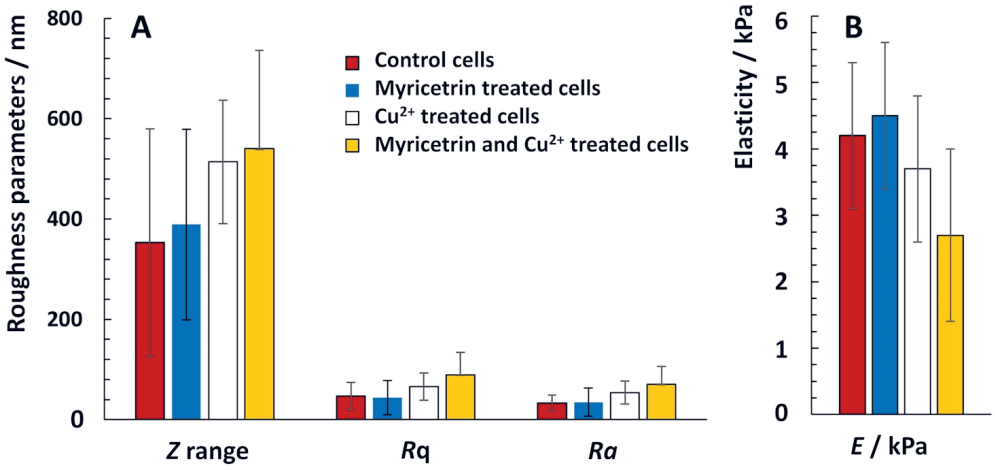

Figure 14. *Roughness parameters (A) and elasticity (B) of treated and untreated neuroblastoma SH-SY5Y cells.*

in *Z*-range being the most pronounced. However, a stronger effect of myricetin was observed in the presence of copper on the topographies of neuroblastoma cells SH-SY5Y, indicating a degeneration of the actin network.

Non-imaging AFM

Since AFM imaging and roughness analysis indicated significant reorganization of the cytoskeleton and filament structures, it made sense to further investigate nanomechanics, i.e., elasticity. Young's moduli measurement results for treated and control cells are shown in Figure 14B. The results show that the myricetin-treated SH-SY5Y cells were stiffer than the control group, while the copper-treated cells were softer than the control cells. Finally, exposure to both copper and myricetin resulted in a significant decrease in cell elasticity (36%) compared to control cells. In conclusion, actin filaments are the major component of the cytoskeleton and cell elasticity is determined by their organization and dynamics. Disorganization of actin filaments reduces the average Young's modulus, demonstrating the importance of actin for the overall mechanical stability of SH-SY5Y cells. AFM is shown to provide biophysical markers for screening neurodegenerative changes as a tool for monitoring cellular integrity.

P19 neuronal cells

The brain is particularly susceptible to oxidative stress due to its enormous oxygen consumption, high polyunsaturated fatty acid content, accumulation of transition metal cations, and limited antioxidant protection *(38)*. Among the various reactive oxygen species (ROS), H_2O_2 is one of the most abundant ROS in aerobic organisms. At concentrations above physiological levels, H_2O_2 can alter the activity of various signaling cascades. Quercetin, a natural flavonol, has exceptional antioxidant activity against various oxidants and other neurotoxic molecules that can induce oxidative stress *(39)*. However, due to its low bioavailability, its concentration is below that required for effective antioxidant activity. Moreover, the physiological function of a cell is closely related to its morphology (40). When the cell physiology changes due to pathological toxins and other substances, its morphology also changes. Therefore, observing and studying the morphological characteristics of cells can serve as a biophysical marker for neuronal changes during induced oxidative stress. Therefore, in our previous study *(41)*, quantitative imaging was performed to obtain the cell topography, and non-imaging AFM provided spatially resolved maps of nanomechanical properties of the cells called cellular elasticity maps. Both approaches provide important information about the cell membranes and the structure of the cytoskeleton. External influences can lead to structural and nanomechanical changes, especially in the organization of microtubules, actin filaments, and neurofilaments. The aim of this research review was to show how the use of AFM can help to investigate changes in the topography and nanomechanical properties of neuronal membranes caused by oxidative stress resulting from drug treatment.

Imaging AFM

All cell imaging and force mapping measurements were performed with neurons fixed in 4% paraformaldehyde. The light microscopy images show the topography of the control neuron soma (Figure 15A), after the treatment with H_2O_2 (Figure 15D), and after the simultaneous exposure to both quercetin and H_2O_2 (Figure 15G). The highest region of the soma is shown on more detailed AFM images (Figure 15B, 15E, 15H) and zoomed topographic images (Figure 15C, 15F, 15I), of control, H_2O_2-treated, and neurons simultaneously treated with both quercetin and H_2O_2, respectively. Isolated control neurons had elongated soma shapes (Figure 15B) with ruffled structures consisting of diverse membrane proteins and membrane folding (Figure1 5C), while neurons exposed to H_2O_2 had irregular circular shapes (Figure 15E), and degenerated cell bodies in which cross-linking of mem-

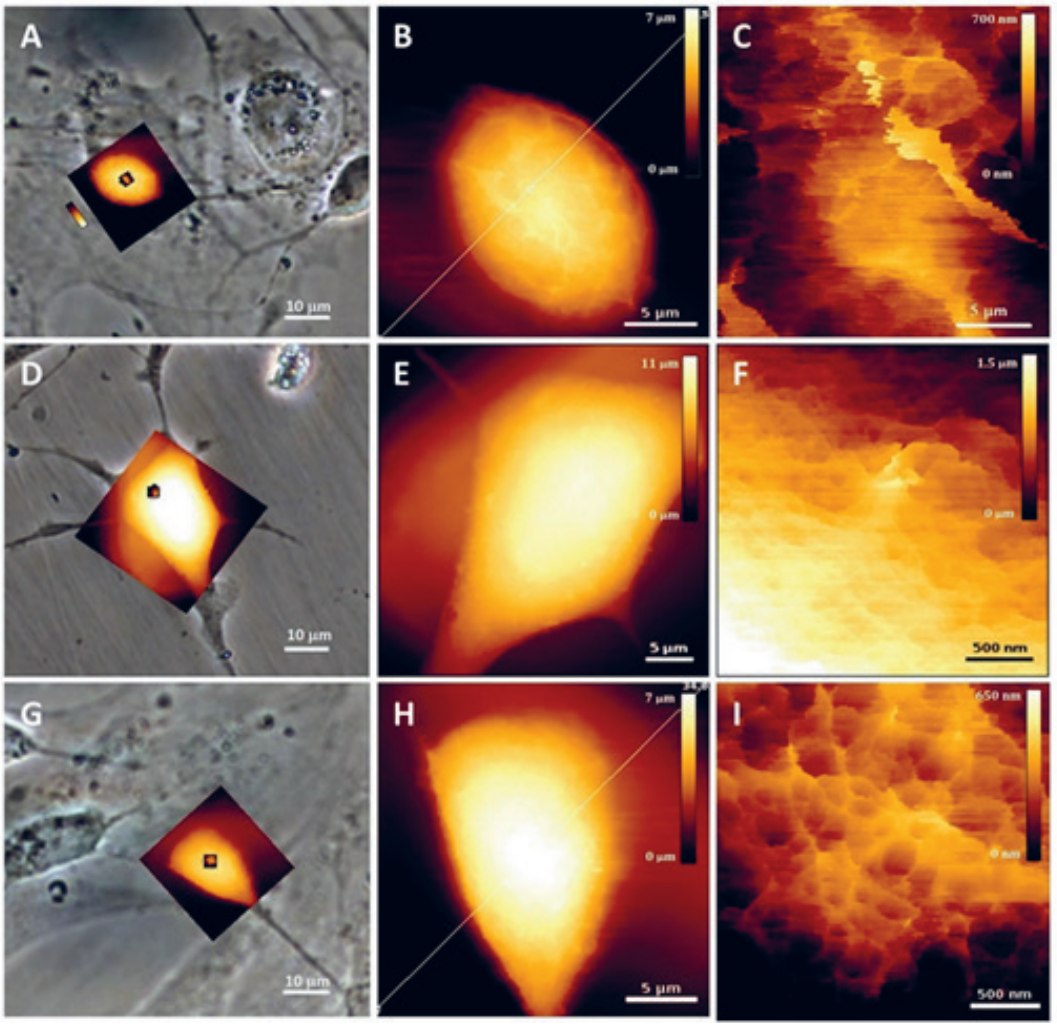

Figure 15. *Light microscopy images of the soma of control neurons (A), of a neuron after treatment with H_2O_2 (D), and after simultaneous exposure to quercetin and H_2O_2 (G). The highest region of the soma is shown on height topographic images (B, E, H), and zoomed (C, F, I), respectively. The scales are indicated on images.*

brane proteins was suppressed (Figure 15F). The shape of P19 neurons treated simultaneously with quercetin and H_2O_2 was more regular (Figure 15H), whereas the fine ruffled assemblies showed only minor modifications, indicating the beneficial effects of quercetin on neuronal morphology (Figure 15I). The spherical crater edges in the control P19 neurons were distinct and sharp (Figure 15C), and significantly disappeared in H_2O_2-treated neurons (Figure 15F). In contrast, in quercetin/H_2O_2 treated neurons they were pitted and became shallow, indicating a minor damage to the cell membrane (Figure 15I). The effects of quercetin and H_2O_2 on morphology (Feret dimensions (*FD*), cell volume (*V*) and cell height (*h*)) and roughness parameters (R_a) at the nanoscale level are summarized in Figure 16A and Figure 16B, respectively.

The data obtained on fixed P19 neurons provided detailed evidence of morphological changes in cellular structures under various treatments. Figure 16 summarizes the H_2O_2-induced decrease in cell volume and decrease in roughness as indicators of cytoskeletal changes. The Feret dimensions of neuronal somas and their height are determined as indicators of an oxidative damage. Indeed, oxidative stress results in an internal structural reorganization of the cytoskeleton, which manifests itself in changes in the shape of the cell as well as in the level of *FD* and height of the cell. For this reason, all observed changes in the above parameters can serve as biophysical markers for the condition of the cells under study. The observed values of FD_{min} and FD_{max} induced by treatment with H_2O_2 and simultaneous treatment with H_2O_2 and quercetin change. FD_{min} increases by 31% and 38% by the treatment with H_2O_2 and simultaneous treatment with H_2O_2 and quercetin, respectively, compared to control cells, indicating that neuronal cells expand (Figure 16A). On the other hand, FD_{max} is reduced by 26% and 30% by treatment with H_2O_2 and simultaneous treatment with H_2O_2 and quercetin, respectively, indicating

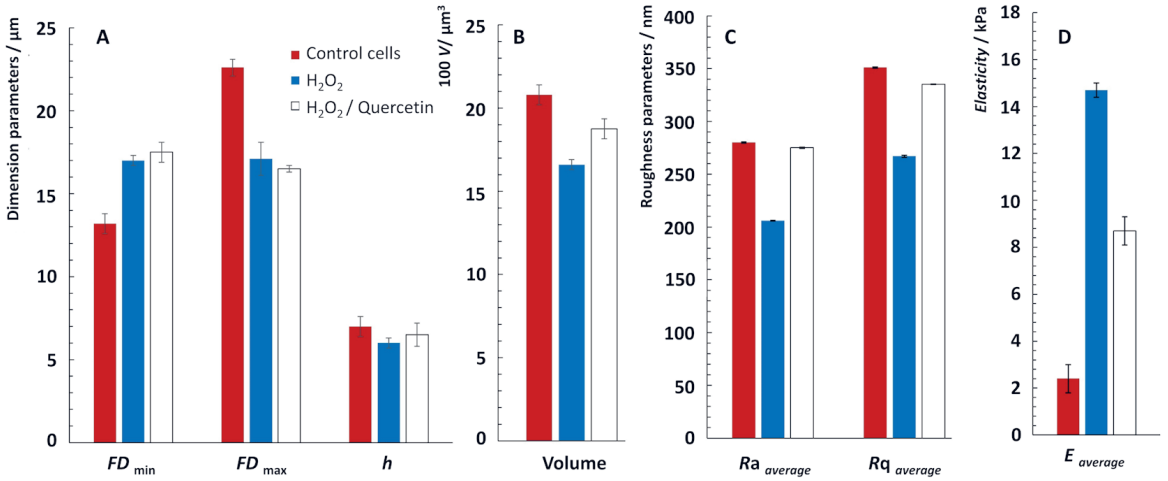

Figure 16. *(A) Feret dimensions and height of cells, (B) cell volume, (C) roughness parameters and (D) elasticity of control and treated neurons.*

that neuronal cells shorten. Neuronal cell height itself decreased by 15% and 10% by treatment with H_2O_2 and simultaneous treatment with H_2O_2 and quercetin, respectively. Based on the changes in the above parameters, the cell volume values were calculated. Thus, the decrease in neuronal volume due to treatment with H_2O_2 was calculated to be 25% compared to control cells, while the effect was reduced to only 5% in the presence of quercetin (Figure 16B). The observed changes in cell volume were suppressed by the presence of quercetin, confirming its neuroprotective role.

The observed morphological changes at the membrane level were also reflected in the pronounced roughness values of the neurons treated with H_2O_2 (Figure 16C). Membrane roughness, which originated from single short and long protein ruffled structures, was decreased in P19 neurons exposed to H_2O_2 but returned to baseline upon simultaneous treatment with H_2O_2 and quercetin. H_2O_2 induced conformational changes in actin structures and promoted the degradation of highly oriented bundles, leading to their shortening, which corresponded with the increase in roughness parameters.

Non-imaging AFM

After analyzing the cell morphology and its changes due to cell treatment, we focused on the cell's nanomechanical properties that reflect the structural reorganization of the cell cytoplasm induced by treatment of neuronal cells with H_2O_2 (± quercetin). The measurements were performed in such a way that the elasticity map of the neuronal cells was measured. The results were statistically analyzed and presented as mean ± SD (Figure 16.D). The control cells have an elasticity of E = (2.2±0.5) kPa. Treatment with H_2O_2 causes a sudden increase in the value of Young's modulus to E = (14.5±1) kPa after 24 hours. In contrast to the cells treated with H_2O_2 only, the neuronal cells treated simultaneously with quercetin and H_2O_2 have an elasticity of E = (8.8±0.9) kPa. This shows that their elasticity increased compared to the control cells, but this increase was much smaller than in cells treated with H_2O_2 alone. By measuring the elasticity of the cells, the protective role of quercetin was confirmed, manifested in the reduction of the effect of H_2O_2 on increasing the cell stiffness.

What could be the cause of the observed changes in their nanomechanical properties when neuronal cells are treated with H_2O_2? The cytoskeletal scaffold of neuronal cells and the connected cortical proteins hold the whole cell relatively tightly together and give it a certain shape and morphology. After treatment of neuronal cells with H_2O_2, reorganization of the entire cytoskeleton was probably induced, primarily in the form of cross-linking of the cortical proteins, resulting in an increase in the stiffness of the cytoskeletal structure. In the presence of quercetin, the internal reorganization of cortical proteins was significantly reduced, i.e., the quercetin prevented the conformational change of important cortical proteins and the actin cytoskeleton in the cytoplasm. In summary, we briefly demonstrated how measuring nanomechanical properties by mapping elasticity in specific regions of P19 neurons can indirectly infer underlying processes at the level of the cytoskeleton in the observed neuronal cell and provide important information in the context of cytotoxicity of substances with therapeutic potential.

CONCLUSION

The many possible applications of AFM for researchers in medicine and life sciences have been described using examples from our earlier studies, which focused on model membranes and cells. AFM as a complementary technique to other biomedical methods is best suited as a tool for screening and monitoring nanomechanical changes at the cellular level. This article thus illustrates the great potential of AFM and its important role in medicine and life science research.

REFERENCES

1. ASMATULU R and KHAN W S 2019 Chapter 13 - Characterization of electrospun nanofibers, In: Asmatulu R and Khan W S (eds) Synthesis and Applications of Electrospun Nanofibers, Elsevier, p 257.
2. ZHANG Y, ZHU W, HUI F, LANZA M, BORCA-TASCIUC T, and MUÑOZ ROJO M 2020 A Review on Principles and Applications of Scanning Thermal Microscopy (SThM). Advanced Functional Materials 30(18): 1900892. https://doi.org/10.1002/adfm.201900892
3. TSENG A A and LI Z 2007 Manipulations of atoms and molecules by scanning probe microscopy. J Nanosci Nanotechnol 7(8): 2582–2595. https://doi.org/10.1166/jnn.2007.624
4. JEMBREK M J, ŠIMIĆ G, HOF P R, and ŠEGOTA S 2015 Atomic force microscopy as an advanced tool in neuroscience. Transl Neurosci 6(1): 117–130. https://doi.org/10.1515/tnsci-2015-0011
5. GIESSIBL F J 2003 Advances in atomic force microscopy. Rev Mod Phys 75(3): 35. https://doi.org/10.1103/RevModPhys.75.949
6. YONGSUNTHON R and LOWER S K 2005 Force Measurements Between a Bacterium and Another Surface In Situ, In: Laskin A I, Bennett J W, Gadd G M, and Sariaslani S (eds) Advances in Applied Microbiology, Academic Press, p 97.
7. ŠEGOTA S, VOJTA D, PLETIKAPIĆ G, and BARANOVIĆ G 2015 Ionic strength and composition govern the elasticity of biological membranes. A study of model DMPC bilayers by force- and transmission IR spectroscopy. Chem Phys Lipids 186: 17–29. https://doi.org/10.1016/j.chemphyslip.2014.11.001
8. MARCHESI A, UMEDA K, KOMEKAWA T, MATSUBARA T, FLECHSIG H, ANDO T, WATANABE S, KODERA N, and FRANZ C M 2021 An ultra-wide scanner for large-area high-speed atomic force microscopy with megapixel resolution. Sci Rep 11(1): 13003. https://doi.org/10.1038/s41598-021-92365-y
9. ÇIFTÇI H T, VERHAGE M, CROMWIJK T, PHAM VAN L, KOOPMANS B, FLIPSE K, and KURNOSIKOV O 2022 Enhancing sensitivity in atomic force microscopy for planar tip-on-chip probes. Microsyst Nanoeng 8(1): 1–11. https://doi.org/10.1038/s41378-022-00379-x
10. SUMBUL F, HASSANPOUR N, RODRIGUEZ-RAMOS J, and RICO F 2020 One-Step Calibration of AFM in Liquid. Frontiers in Physics 8: 301. https://doi.org/10.3389/fphy.2020.00301
11. SCHÖNHERR H and VANCSO G J 2010 Atomic Force Microscopy in Practice, In: Schönherr H and Vancso G J (eds) Scanning Force Microscopy of Polymers, Springer, Berlin, Heidelberg, p 25.
12. MORRIS, MICHAEL D. V J, KIRBY A R, and GUNNING A P 2009 Basic principles, In: Atomic Force Microscopy for Biologists, IMPERIAL COLLEGE PRESS, p 41.
13. HÖLSCHER H 2012 AFM, Tapping Mode, In: Bhushan B (ed) Encyclopedia of Nanotechnology, Springer Netherlands, Dordrecht, p 99.
14. QUINTANILLA M A S 2013 Surface Analysis Using Contact Mode AFM, In: Wang Q J and Chung Y-W (eds) Encyclopedia of Tribology, Springer US, Boston, MA, p 3401.
15. SADŽAK A, BRKLJAČA Z, CRNOLATAC I, BARANOVIĆ G, and ŠEGOTA S 2020 Flavonol clustering in model lipid membranes: DSC, AFM, force spectroscopy and MD simulations study. Colloids Surf B Biointerfaces 193: 111147. https://doi.org/10.1016/j.colsurfb.2020.111147
16. SADŽAK A, MRAVLJAK J, MALTAR-STRMEČKI N, ARSOV Z, BARANOVIĆ G, ERCEG I, KRIECHBAUM M, STRASSER V, PŘIBYL J, and ŠEGOTA S 2020 The Structural Integrity of the Model Lipid Membrane during Induced Lipid Peroxidation: The Role of Flavonols in the Inhibition of Lipid Peroxidation. Antioxidants 9(5): 430. https://doi.org/10.3390/antiox9050430
17. MANDIĆ L, SADŽAK A, STRASSER V, BARANOVIĆ G, DOMAZET JURAŠIN D, DUTOUR SIKIRIĆ M, and ŠEGOTA S 2019 Enhanced Protection of Biological Membranes during Lipid Peroxidation: Study of the Interactions between Flavonoid Loaded Mesoporous Silica Nanoparticles and Model Cell Membranes. IJMS 20(11): 2709. https://doi.org/10.3390/ijms20112709
18. ŠEGOTA S, VOJTA D, KENDZIORA D, AHMED I, FRUK L, and BARANOVIĆ G 2015 Ligand-Dependent Nanoparticle Clustering within Lipid Membranes Induced by Surrounding Medium. J Phys Chem B 119(16): 5208–5219. https://doi.org/10.1021/acs.jpcb.5b00898
19. NAGAO E and DVORAK J A 1999 Phase imaging by atomic force microscopy: analysis of living homoiothermic vertebrate cells. Biophys J 76(6): 3289–3297. https://doi.org/10.1016/S0006-3495(99)77481-3
20. HÖLSCHER H 2012 AFM, Non-contact Mode, In: Bhushan B (ed) Encyclopedia of Nanotechnology, Springer Netherlands, Dordrecht, p 93.
21. BORZEA C and COMEAGĂ D 2018 Adjusting the Resonant Frequency of a Cantilever Piezoelectric Harvester. Turbo V(2): 11–18.
22. HIGGINS M J, SADER J E, and JARVIS S P 2006 Frequency Modulation Atomic Force Microscopy Reveals Individual Intermediates Associated with each Unfolded I27 Titin Domain. Biophys J 90(2): 640–647. https://doi.org/10.1529/biophysj.105.066571
23. GARCÍA R 2010 Theory of Amplitude Modulation AFM, In: Amplitude Modulation Atomic Force Microscopy, John Wiley & Sons, Ltd, p 41.
24. OLIVEIRA R R L D, ALBUQUERQUE D a. C, CRUZ T G S, YAMAJI F M, LEITE F L, OLIVEIRA R R L D, ALBUQUERQUE D a. C, CRUZ T G S, YAMAJI F M, and LEITE F L 2012 Measurement of the Nanoscale Roughness by Atomic Force Microscopy: Basic Principles and Applications, In: Measurement of the Nanoscale Roughness by Atomic Force Microscopy: Basic Principles and Applications, IntechOpen,
25. ANTONINI S, CAPPELLUTI M A, MEUCCI S, JACCHETTI E, VITTORIO O, PARCHI P, LISANTI M, PACINI S, PETRINI M, BELTRAM F AND CECCHINI M 2014 Human Mesenchymal Stromal Cell Enhanced Morphological Polarization by Contact Interaction with Polyethylene Terephthalate Nanogratings. Curr. Nanosci. 10 (6): 773–778. https://doi.org/10.2174/1573413710666140815205825
26. MÜLLER D J, DUMITRU A C, LO GIUDICE C, GAUB H E, HINTERDORFER P, HUMMER G, DE YOREO J J, DUFRÊNE Y F, and ALSTEENS D 2021 Atomic Force Microscopy-Based Force Spectroscopy and Multiparametric Imaging of Biomolecular and Cellular Systems. Chem Rev 121(19): 11701–11725. https://doi.org/10.1021/acs.chemrev.0c00617
27. ZLATANOVA J, LINDSAY S M, and LEUBA S H 2000 Single molecule force spectroscopy in biology using the atomic force microscope. Prog Biophys Mol Biol 74(1–2): 37–61. https://doi.org/10.1016/s0079-6107(00)00014-6
28. GARCÍA R and PÉREZ R 2002 Dynamic atomic force microscopy methods. Surface Science Reports 47(6): 197–301. https://doi.org/10.1016/S0167-5729(02)00077-8
29. BUGACOV A, RESCH R, BAUR C, MONTOYA N, WORONOWICZ K, PAPSON A, KOEL B E, REQUICHA A, and WILL P 1999 Measuring the tip-sample separation in dynamic force microscopy. Probe Microscopy 1(4): 345–354. Available at: https://collaborate.princeton.edu/en/publications/measuring-the-tip-sample-separation-in-dynamic-force-microscopy
30. TIAN X, HE X, SONG D, LI Z, KHAN M, LIU H, and QIU L 2022 AFM characterization of surface mechanical and electrical properties of some common rocks. International Journal of Mining Science and Technology 32(2): 435–445. https://doi.org/10.1016/j.ijmst.2021.12.008

31. HALL D, LEE S Y, MEZIANE T 2006 Fatty acids as trophic tracers in an experimental estuarine food chain: tracer transfer. J. Exp. Marine Biol. Ecol. 336: 42–53. https://doi.org/10.1016/j.jembe.2006.04.004

32. PETRACHE H I, TRISTRAM-NAGLE S, NAGLE J F 1998 Fluid phase structure of EPC and DMPC bilayers. Chem. Phys. Lipids 95: 83–94. https://doi.org/10.1016/S0009-3084(98)00068-1

33. STUMM W, MORGAN J J 1996 Aquatic Chemistry, Environmental Science and Technology. John Wiley & Sons, Inc., New York, pp. 899.

34. SADŽAK A, VLAŠIĆ I, KIRALJ Z, BATARELO M, ORŠOLIĆ N, JAZVINŠĆAK JEMBREK M, KUŠEN I, and ŠEGOTA S 2021 Neurotoxic Effect of Flavonol Myricetin in the Presence of Excess Copper. Molecules 26(4): 845. https://doi.org/10.3390/molecules26040845

35. SAPORITO-MAGRIÑÁ C M, MUSACCO-SEBIO R N, ANDRIEUX G, KOOK L, ORREGO M T, TUTTOLOMONDO M V, DESIMONE M F, BOERRIES M, BORNER C, REPETTO M G 2018 Copper-induced cell death and the protective role of glutathione: The implication of impaired protein folding rather than oxidative stress. Metallomics 10: 1743–1754. https://doi.org/10.1039/c8mt00182k

36. CAO G, SOfiC E, PRIOR R L 1997 Antioxidant and prooxidant behavior of flavonoids: Structure-activity relationships. Free Radic. Biol. Med. 22: 749–760. https://doi.org/10.1016/S0891-5849(96)00351-6

37. SEMWAL D K, SEMWAL R B, COMBRINCK S, VILJOEN A 2016 Myricetin: A dietary molecule with diverse biological activities. Nutrients 8: 90. https://doi.org/10.3390/nu8020090

38. WANG X, MICHAELIS E K 2010 Selective neuronal vulnerability to oxidative stress in the brain. Front Aging Neurosci. 2: 12. https://doi.org/10.3389/fnagi.2010.00012

39. DAJAS F Life or death: neuroprotective and anticancer effects of quercetin. J Ethnopharmacol. 2012; 143: 383–396. https://doi.org/10.1016/j.jep.2012.07.005

40. ROSSO G, LIASHKOVICH I, SHAHIN V 2019 In Situ Investigation of Interrelationships Between Morphology and Biomechanics of Endothelial and Glial Cells and their Nuclei. Adv Sci. 6(1): 1801638. https://doi.org/10.1002/advs.201801638

41. JAZVINŠĆAK JEMBREK M, VLAINIĆ J, ČADEŽ V and ŠEGOTA 2018 Atomic force microscopy reveals new biophysical markers for monitoring subcellular changes in oxidative injury: Neuroprotective effects of quercetin at the nanoscale. PLoS One 13(10): e0200119. https://doi.org/10.1371/journal.pone.0200119